J. Fluid Mech. (1997), *vol.* 350, *pp.* 311–330. Printed in the United Kingdom

Instability and transient growth for two trailing-vortex pairs

By J. D. CROUCH

Boeing Commercial Airplane Group, PO Box 3707, Seattle, WA 98124-2207, USA

(Received 23 December 1996 and in revised form 18 June 1997)

The stability of two vortex pairs is analysed as a model for the vortex system generated by an aircraft in flaps-down configuration. The co-rotating vortices on the starboard and port sides tumble about one another as they propagate downward. This results in a time-periodic basic state for the stability analysis. The dynamics and instability of the trailing vortices are modelled using thin vortex filaments. Stability equations are derived by matching the induced velocities from Biot–Savart integrals with kinematic equations obtained by temporal differentiation of the vortex position vectors. The stability equations are solved analytically as an eigenvalue problem, using Floquet theory, and numerically as an initial value problem. The instabilities are periodic along the axes of the vortices with wavelengths that are large compared to the size of the vortex cores. The results show symmetric instabilities that are linked to the long-wavelength Crow instability. In addition, new symmetric and antisymmetric instabilities are observed at shorter wavelengths. These instabilities have growth rates 60–100% greater than the Crow instability. The system of two vortex pairs also exhibits transient growth which can lead to growth factors of 10 or 15 in one-fifth of the time required for the same growth due to instability.

1. Introduction

Trailing vortices in the wake of aircraft play an important role in determining the capacity of commercial airports. One of the dominant mechanisms affecting the persistence of these vortices is instability. The growth of sinusoidal instabilities along the vortex axes can lead to large distortions and the ultimate breakup of the vortices. When the vortex distortions are large enough, the counter-rotating vortices touch and pinch off to form vortex rings which then degenerate into smaller-scale turbulence.

The evolution of the sinusoidal instabilities on a single pair of trailing vortices was analysed by Crow (1970). Predictions from Crow's analysis are in good agreement with observations of aircraft in flight. For an aircraft with an elliptically loaded wing, Crow estimates the most-amplified wavelength to be about 8 times the vortex spacing. The instability growth is relatively weak from a practical point of view: the instability amplitude increases by a factor of 2.3 during the time the vortices propagate a distance equal to their spacing. This leads to a strong sensitivity to the initial amplitudes of disturbances. Nonetheless, the instability can break up the vortices well before they are expected to decay due to other means.

Under natural conditions, the vortices are excited due to turbulence in the atmosphere. The time required to break up the vortices then depends on the strength of the atmospheric turbulence in addition to the instability growth rate. The analysis

of Crow & Bate (1976) predicts the average time to break up as a function of the turbulent dissipation. This analysis is in general agreement with the average time to break up observed in the experiments of Sarpkaya & Daly (1987) and the numerical simulations of Spalart & Wray (1996). However, the experiments and simulations show that variations from the average are quite large. This stems from the strong sensitivity to initial amplitudes that results from the relatively weak growth rates, and from the randomness of the turbulent forcing.

These studies did not account for the multiple vortices that exist for some distance behind aircraft during take off and landing. Commercial aircraft under flaps-down conditions may produce a number of vortices along the span. Many of these vortices quickly merge due to their close proximity and large effective core sizes. However, distinct vortices associated with the outboard edge of the inboard flap and the wing tip can persist much longer.

1.1. *Persistence of multiple vortices*

The time to merger is still not well predicted for realistic configurations at flight Reynolds numbers. Inviscid studies predict an infinite time to merger for a co-rotating vortex pair with core sizes which are small relative to the separation distance (Rossow 1977). Observations based on tracer materials in towing-tank experiments show merger of the flap-edge and tip vortices after the vortices propagate a distance of approximately one span (Dunham 1974). The early merger observed in these experiments is probably due to large core sizes resulting from lower Reynolds numbers and turbulence in the initial shear layer.

Results from flight tests have not definitively characterized the time to merger for the flap and tip vortices. Some flight tests show distinct vortices after a propagation distance of several spans; in other cases, only a single pair is detected (Snedeker & Bilanin 1975). In these flight tests, multiple vortices are only observed for the upwind set of vortices (the vortices were carried past a measurement tower by a side wind). Analysis of flight data, carried out by Caiger & Gould (1971), suggest distinct co-rotating vortices after a propagation distance of nearly 2 spans. The time to merger depends strongly on the configuration (i.e. the size and spacing of the initial vortex cores) among other factors.

More recent results suggest that distinct vortex pairs may persist well downstream of an aircraft in flaps-down configuration. Water-tunnel and towing-tank experiments of Fell & Staufenbiel (1995) show very distinct flap-edge and wing-tip vortices which propagate consistent with numerical solution of the vorticity transport equation. Their model produced a counter-rotating vortex at the inboard edge of the flap, in addition to the co-rotating flap and tip vortices produced outboard. However, their results are limited to approximately 6 spans behind the aircraft. The wind-tunnel experiments of de Bruin *et al.* (1996) on an airplane model in a flaps-down configuration show distinct flap-edge and wing-tip vortices 13 spans downstream of the aircraft. (Their results at 13 spans were presented orally, the paper only contains results up to 4.7 spans.) Field surveys at this location show the vorticity to be concentrated in distinct vortices. The early dynamics of the vortices are well described by numerical solutions of the two-dimensional vorticity transport equation. Comparisons between the experiment and simulation suggest that the vortices will continue to remain distinct much further downstream. Recent towing-tank experiments of Jacob & Savas (1997) show distinct flap-edge and wing-tip vortices up to about one period of their co-rotation. However, these experiments do not include thrust effects which may also influence the co-rotating vortex merger.

1.2. *Instability of multiple vortices*

Independent of the actual time to merger, the initial development of perturbations occurs on the system of multiple vortices. We consider the stability of a vortex system with two dominant vortex pairs. This assumes that vortices produced by outboard-flap edges quickly merge with the tip vortices as suggested by experiments. The counter-rotating vortices at the side of the body are not included, but their inclusion would not significantly alter the results. Any asymmetry in the vortex system, due for example to corrections in the flight path, are neglected. These assumptions are exploited in the analysis, but they are not required for the numerical initial-value calculations.

Consideration of the two-vortex-pair system offers the potential for identifying new instabilities and growth mechanisms which may be relevant to the break up of the vortices. Hackett & Evans (1977) considered different scenarios to describe the evolution of multiple vortex pairs, but their work did not include a study of the stability of the multiple-vortex system. Klein, Majda & Damodaran (1995) have developed a general formulation for the stability of an arbitrary number of vortex filaments. Their detailed analysis and results, however, focus on the linear and nonlinear stability of a single vortex pair. Their linear results are in agreement with Crow's analysis for counter-rotating vortices and with Jimenez's results for co-rotating vortices (Jimenez 1975).

Following the formulation of Crow (1970), we provide a detailed analysis of the two-vortex-pair system – including both linear stability and transient growth. Some results of this analysis were initially presented in the recent AGARD Symposium on trailing vortices (Crouch 1996). The vortices are represented by thin filaments, and the local singularities in the Biot–Savart integrals are removed using a cutoff approximation. Details of the formulation and analysis leading to the stability equations are given in §2. Section 3 describes the Floquet analysis and the analysis of the transient growth. The results of these analyses are presented in §4. Results from numerical integration of the stability equations are given in §5, and conclusions are discussed in §6.

2. Formulation of stability equations

The motion of the vortex pairs can be characterized by a mean propagation and a co-rotation, resulting in a tumbling effect. For real configurations, the co-rotation begins as the vortices roll up – producing helical structures along the line of the circulation centroids on the starboard and port sides. The wavelength of the helix is $2\pi\widetilde{V}_A/\widetilde{\omega}$, where $\widetilde{\omega}$ is the vortex-pair rotation frequency and $\widetilde{V}_A$ is the aircraft speed. Our analysis assumes the helix wavelength is large relative to the instability wavelength and thus the helical variation can be neglected. The relative position of the vortices is then independent of the axial distance and dependent only on time.

The dynamics of the trailing vortices are modelled using thin vortex filaments. The formulation follows the original work of Crow (1970) for the stability of a single vortex pair. Figure 1 is a schematic of the trailing-vortex system. The local coordinate system moves with the mean position of the vortices. The vortices that are initially outboard are designated 1 and 2, and the inboard vortices 3 and 4. The total positive circulation (produced by one wing) is given by $\widetilde{\Gamma}_0 = \widetilde{\Gamma}_2 + \widetilde{\Gamma}_4$, where $\widetilde{\Gamma}_2$ and $\widetilde{\Gamma}_4$ characterize the strengths of the two vortex pairs and $\widetilde{\Gamma}_1 = -\widetilde{\Gamma}_2$, $\widetilde{\Gamma}_3 = -\widetilde{\Gamma}_4$. The circulation centroids on the starboard and port sides are separated by a distance $\tilde{b}$ and the co-rotating vortices are separated by a distance $\tilde{d}$. All quantities are non-dimensionalized by the

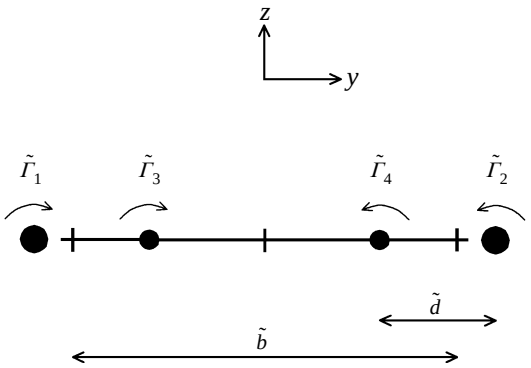

FIGURE 1. Schematic showing the initial positions of the vortices.

length scale $\tilde{b}$ and time scale $2\pi\tilde{b}^2/\tilde{\Gamma}_0$. A non-dimensional time of $t = 1$ corresponds to the time required for the vorticity centroids to propagate a distance equal to their spacing $\tilde{b}$. This non-dimensionalization leads to two key parameters characterizing the system: $\Gamma \equiv \tilde{\Gamma}_4/\tilde{\Gamma}_2$ and $\delta \equiv \tilde{d}/\tilde{b}$. In non-dimensional terms, the circulation strengths become $\Gamma_2 = -\Gamma_1 = 1/(1+\Gamma)$, $\Gamma_4 = -\Gamma_3 = \Gamma/(1+\Gamma)$.

When δ is small the vortices rotate in a near-circular path (in the local frame) with frequency $\omega = 1/\delta^2$. As δ is increased, the vortex trajectories become distorted and the frequency is reduced below $1/\delta^2$. The vortices are perturbed by an axially periodic disturbance with wavelength $\lambda = 2\pi/\alpha$. Neglecting the helical variation of the vortices requires that $1/(V_A\alpha\delta^2) \ll 1$, where V_A is the aircraft speed non-dimensionalized by the mean vortex propagation velocity; a typical value is $V_A \approx 50$.

2.1. *Induced velocities*

Equations for the propagation and stability of the vortices are derived by matching the induced velocities from Biot–Savart integrals with kinematic equations obtained by temporal differentiation of the vortex position vectors. The position vector representing the location of induced velocity on vortex n is given by

$$\boldsymbol{r}_n = x_n\hat{\boldsymbol{i}} + (y_n + \eta_n e^{i\alpha x_n})\hat{\boldsymbol{j}} + (z_n + \zeta_n e^{i\alpha x_n})\hat{\boldsymbol{k}}, \tag{2.1}$$

with n taking values from 1 to 4. The position vector representing the induction source has the same form but the subscript n is replaced by m. The induced velocity at $\boldsymbol{r}_n$ is given by

$$\boldsymbol{v}_n = \sum_{m=1}^{4} \frac{\Gamma_m}{2} \int_{-\infty}^{\infty} \frac{(\boldsymbol{r}_m - \boldsymbol{r}_n)}{|\boldsymbol{r}_m - \boldsymbol{r}_n|^3} \times \frac{\partial \boldsymbol{r}_m}{\partial x_m} \mathrm{d}x_m, \tag{2.2}$$

where

$$\boldsymbol{r}_m - \boldsymbol{r}_n = x_{mn}\hat{\boldsymbol{i}} + (y_{mn} + \eta_m e^{i\alpha x_m} - \eta_n e^{i\alpha x_n})\hat{\boldsymbol{j}} + (z_{mn} + \zeta_m e^{i\alpha x_m} - \zeta_n e^{i\alpha x_n})\hat{\boldsymbol{k}}, \tag{2.3}$$

and $x_{mn} = x_m - x_n$, $y_{mn} = y_m - y_n$, $z_{mn} = z_m - z_n$. Expanding the integrand of (2.2), the induced velocity can be written in the form

$$\boldsymbol{v}_n = \sum_{m=1}^{4} \Big\{ V_{0mn}\hat{\boldsymbol{j}} + W_{0mn}\hat{\boldsymbol{k}} + \big(V_{1mn}\zeta_n + V_{2mn}\zeta_m + V_{3mn}\eta_n + V_{4mn}\eta_m\big)e^{i\alpha x_n}\hat{\boldsymbol{j}} + \big(W_{1mn}\eta_n + W_{2mn}\eta_m + W_{3mn}\zeta_n + W_{4mn}\zeta_m\big)e^{i\alpha x_n}\hat{\boldsymbol{k}} \Big\}. \tag{2.4}$$

Equation (2.4) is linearized based on the assumption that the perturbation amplitudes are small relative to the minimum separation distance of the vortices ($|\eta_n|/\delta \ll 1$, $|\zeta_n|/\delta \ll 1$ for the range of parameters considered). The velocity components V_{imn} and W_{imn} are given by integrals defined as

$$V_{0mn} = \Gamma_m \int_0^\infty r^{-3} z_{mn} \, \mathrm{d}x, \tag{2.5}$$

$$W_{0mn} = \Gamma_m \int_0^\infty -r^{-3} y_{mn} \, \mathrm{d}x, \tag{2.6}$$

$$V_{1mn} = \Gamma_m \int_0^\infty (-r^{-3} + 3r^{-5} z_{mn}^2) \, \mathrm{d}x, \tag{2.7}$$

$$V_{2mn} = \Gamma_m \int_0^\infty (r^{-3}(1 - \mathrm{i}\alpha x) - 3r^{-5} z_{mn}^2) \mathrm{e}^{\mathrm{i}\alpha x} \, \mathrm{d}x, \tag{2.8}$$

$$V_{3mn} = \Gamma_m \int_0^\infty 3r^{-5} y_{mn} z_{mn} \, \mathrm{d}x, \tag{2.9}$$

$$V_{4mn} = \Gamma_m \int_0^\infty -3r^{-5} y_{mn} z_{mn} \mathrm{e}^{\mathrm{i}\alpha x} \, \mathrm{d}x, \tag{2.10}$$

$$W_{1mn} = \Gamma_m \int_0^\infty (r^{-3} - 3r^{-5} y_{mn}^2) \, \mathrm{d}x, \tag{2.11}$$

$$W_{2mn} = \Gamma_m \int_0^\infty (-r^{-3}(1 - \mathrm{i}\alpha x) + 3r^{-5} y_{mn}^2) \mathrm{e}^{\mathrm{i}\alpha x} \, \mathrm{d}x, \tag{2.12}$$

$$W_{3mn} = \Gamma_m \int_0^\infty -3r^{-5} y_{mn} z_{mn} \, \mathrm{d}x, \tag{2.13}$$

$$W_{4mn} = \Gamma_m \int_0^\infty 3r^{-5} y_{mn} z_{mn} \mathrm{e}^{\mathrm{i}\alpha x} \, \mathrm{d}x, \tag{2.14}$$

where $r = [x_{mn}^2 + y_{mn}^2 + z_{mn}^2]^{1/2}$ and $x = x_{mn}$. The factor $1/2$ in (2.2) is removed and the integration is taken from 0 to ∞.

For $n \neq m$, the integrals (2.5)–(2.14) provide the contributions to the mutual induction. These integrals can be evaluated analytically to yield

$$V_{0mn} = \Gamma_m \left(\frac{z_{mn}}{r^2} \right), \tag{2.15}$$

$$W_{0mn} = \Gamma_m \left(-\frac{y_{mn}}{r^2} \right), \tag{2.16}$$

$$V_{1mn} = \Gamma_m \left(-\frac{1}{r^2} + \frac{2z_{mn}^2}{r^4} \right), \tag{2.17}$$

$$V_{2mn} = \Gamma_m \left(\frac{\alpha}{r} K_1(\alpha r) + \alpha^2 K_0(\alpha r) - \frac{z_{mn}^2 \alpha^2}{r^2} K_2(\alpha r) \right), \tag{2.18}$$

$$V_{3mn} = \Gamma_m \left(\frac{2y_{mn} z_{mn}}{r^4} \right), \tag{2.19}$$

$$V_{4mn} = \Gamma_m \left(-\frac{y_{mn} z_{mn} \alpha^2}{r^2} K_2(\alpha r) \right), \tag{2.20}$$

$$W_{1mn} = \Gamma_m \left(\frac{1}{r^2} - \frac{2y_{mn}^2}{r^4} \right), \tag{2.21}$$

$$W_{2mn} = \Gamma_m \left(-\frac{\alpha}{r} K_1(\alpha r) - \alpha^2 K_0(\alpha r) + \frac{y_{mn}^2 \alpha^2}{r^2} K_2(\alpha r) \right), \tag{2.22}$$

$$W_{3mn} = \Gamma_m \left(-\frac{2y_{mn} z_{mn}}{r^4} \right), \tag{2.23}$$

$$W_{4mn} = \Gamma_m \left(\frac{y_{mn} z_{mn} \alpha^2}{r^2} K_2(\alpha r) \right). \tag{2.24}$$

The functions $K_0(\alpha r)$, $K_1(\alpha r)$, and $K_2(\alpha r)$ are modified Bessel functions of the second kind.

For $m = n$, the integrals (2.5)–(2.14) contain a non-physical singularity at $x = 0$ due to the thin-filament approximation. This singularity can be removed by introducing a cutoff distance x_0 which accounts for the finite core of the vortices. Evaluating the integrals over the interval $[x_0, \infty)$ then yields

$$V_{0nn} = W_{0nn} = V_{3nn} = V_{4nn} = W_{3nn} = W_{4nn} = 0, \tag{2.25}$$

$$V_{1nn} = \frac{\Gamma_n}{2} \left(-\frac{1}{x_0^2} \right), \tag{2.26}$$

$$V_{2nn} = \frac{\Gamma_n}{2} \left(\frac{\cos \alpha x_0}{x_0^2} + \frac{\alpha \sin \alpha x_0}{x_0} - \alpha^2 \mathrm{Ci}(\alpha x_0) \right), \tag{2.27}$$

$$W_{1nn} = \frac{\Gamma_n}{2} \left(\frac{1}{x_0^2} \right), \tag{2.28}$$

$$W_{2nn} = \frac{\Gamma_n}{2} \left(-\frac{\cos \alpha x_0}{x_0^2} - \frac{\alpha \sin \alpha x_0}{x_0} + \alpha^2 \mathrm{Ci}(\alpha x_0) \right), \tag{2.29}$$

where $\mathrm{Ci}(\alpha x_0)$ is the cosine integral. The cutoff parameter x_0 can be related to the effective core diameter c_e by the expression $x_0 = 0.3210 c_e$ (Crow 1970; Widnall 1975). Widnall, Bliss & Zalay (1971) have shown that any compact vorticity distribution can be represented by a Rankine vortex with the proper choice of the effective core size. The value of the core size (or the cutoff parameter) is set by matching the azimuthal kinetic energy between the arbitrary vorticity distribution and the Rankine vortex. Axial velocity within the vortex can also be accounted for using the cutoff parameter (Widnall *et al.* 1971; Moore & Saffman 1972).

The results of §§4 and 5 are given in terms of a cutoff parameter ϵ, which characterizes the cores of the outboard vortices ($x_0 = \epsilon$ for $n = 1, 2$). The cutoff distance for the inboard vortices is scaled in relation to their circulation level ($x_0 = \epsilon \Gamma^{1/2}$, for $n = 3, 4$). This assumes that differences in circulation are due to differences in the core size, and that the peak vorticity and vorticity distribution are fixed. Assumptions about the relative core sizes for the inboard and outboard vortices do not affect any of the general results and conclusions to be presented. However, the quantitative results which show sensitivity to the cutoff parameter will also be sensitive the choice of relative core sizes.

2.2. *Stability equations*

The induced motion of the trailing vortices satisfies a kinematic condition derived from the temporally varying position vector. In the absence of any constraints on the

vortex motions,

$$\frac{\partial \boldsymbol{r}_{Fn}}{\partial t} = W_0 \hat{\boldsymbol{k}} + \frac{\partial \boldsymbol{r}_n}{\partial t} = \boldsymbol{v}_n. \tag{2.30}$$

The vector $\boldsymbol{r}_{Fn}$ is measured from a fixed frame and W_0 is the propagation velocity for the local reference frame (i.e. $W_0 = 1$, the small-δ mean propagation velocity of the vortices). Differentiating (2.1) with respect to t yields

$$\frac{\mathrm{d}\boldsymbol{r}_n}{\mathrm{d}t} = \left(\frac{\mathrm{d}y_n}{\mathrm{d}t} + \frac{\mathrm{d}\eta_n}{\mathrm{d}t}\mathrm{e}^{\mathrm{i}\alpha x_n}\right)\hat{\boldsymbol{j}} + \left(\frac{\mathrm{d}z_n}{\mathrm{d}t} + \frac{\mathrm{d}\zeta_n}{\mathrm{d}t}\mathrm{e}^{\mathrm{i}\alpha x_n}\right)\hat{\boldsymbol{k}}. \tag{2.31}$$

Combining (2.4), (2.30) and (2.31), the equations for the mean vortex positions become

$$\frac{\mathrm{d}y_n}{\mathrm{d}t} = \sum_{m=1}^{4} V_{0mn}, \tag{2.32}$$

$$\frac{\mathrm{d}z_n}{\mathrm{d}t} = \sum_{m=1}^{4} W_{0mn} - W_0, \tag{2.33}$$

with initial conditions defined as

$$\left.\begin{aligned} &y_2(0) = 1/2 + \delta\Gamma/(1+\Gamma),\ y_4(0) = 1/2 - \delta/(1+\Gamma), \\ &y_1(0) = -y_2(0),\ y_3(0) = -y_4(0),\ z_n(0) = 0,\ n = 1,4. \end{aligned}\right\} \tag{2.34}$$

The perturbation amplitudes are governed by

$$\frac{\mathrm{d}\eta_n}{\mathrm{d}t} = \sum_{m=1}^{4}(V_{3mn}\eta_n + V_{4mn}\eta_m + V_{1mn}\zeta_n + V_{2mn}\zeta_m), \tag{2.35}$$

$$\frac{\mathrm{d}\zeta_n}{\mathrm{d}t} = \sum_{m=1}^{4}(W_{1mn}\eta_n + W_{2mn}\eta_m + W_{3mn}\zeta_n + W_{4mn}\zeta_m), \tag{2.36}$$

with initial conditions

$$\eta_n(0) = \eta_{n0},\ \zeta_n(0) = \zeta_{n0}. \tag{2.37}$$

The amplitude equations (2.35) and (2.36) are a set of eight coupled differential equations. The coefficients (V_{imn}, W_{imn}) are periodic functions of time due to the co-rotation of the vortex pair. When $\Gamma = 0$, the equations reduce to those considered by Crow (1970).

3. Stability and transient-growth analyses

Equations (2.32)–(2.37) can be solved by a combination of analytical and numerical methods to yield the stability characteristics for the system of two vortex pairs. Introducing the disturbance vector $\boldsymbol{\phi} = (\eta_1, \eta_2, \eta_3, \eta_4, \zeta_1, \zeta_2, \zeta_3, \zeta_4)^T$, equations (2.35) and (2.36) can be written in the compact form

$$(\mathrm{d}/\mathrm{d}t)\boldsymbol{\phi} = [\boldsymbol{F}(t)]\boldsymbol{\phi}. \tag{3.1}$$

The elements of the matrix $[\boldsymbol{F}(t)]$ depend on time through the changing vortex positions given by (2.32)–(2.34). Thus $[\boldsymbol{F}(t)]$ satisfies the condition $[\boldsymbol{F}(t+T)] = [\boldsymbol{F}(t)]$, where T is the rotation period for the co-rotating pair; $T \approx 2\pi\delta^2$ for small δ. The vortex positions and the coefficient matrix $[\boldsymbol{F}(t)]$ are characterized by the parameters Γ, δ, and ϵ.

3.1. *Floquet theory*

The growth rate for instability can be determined from (3.1) using the Floquet theory (Nayfeh & Mook 1979). We first define a non-singular constant matrix $[\boldsymbol{A}]$ by numerically integrating (3.1) over one period of the vortex rotation. Using $\boldsymbol{\phi}(0) = (1,0,0,0,0,0,0,0)^T$ as an initial condition, the resulting vector after integration provides the first column of $[\boldsymbol{A}]$, $a_1 = \boldsymbol{\phi}(T)$. Likewise, setting the kth element of $\boldsymbol{\phi}(0)$ to 1 with all others zero yields the kth column a_k. The disturbance vector after one period of evolution $\boldsymbol{\phi}(t+T)$ can then be related to the disturbance vector $\boldsymbol{\phi}(t)$ through the relation

$$\boldsymbol{\phi}(t+T) = [\boldsymbol{A}]\boldsymbol{\phi}(t). \tag{3.2}$$

Introducing $\boldsymbol{\phi}(t) = [\boldsymbol{P}]\boldsymbol{\psi}(t)$ into (3.2), where the columns of $[\boldsymbol{P}]$ are unit norm eigenvectors of $[\boldsymbol{A}]$, leads to

$$\boldsymbol{\psi}(t+T) = [\boldsymbol{P}]^{-1}[\boldsymbol{A}][\boldsymbol{P}]\boldsymbol{\psi}(t) = [\boldsymbol{S}]\boldsymbol{\psi}(t). \tag{3.3}$$

Assuming the eigenvalues of $[\boldsymbol{A}]$ are distinct, the matrix $[\boldsymbol{S}]$ is diagonal with the eigenvalues σ as its entries. For a given eigenvalue, $\boldsymbol{\psi}(t+nT) = \sigma^n\boldsymbol{\psi}(t)$, or more generally,

$$\boldsymbol{\psi}(t+nT) = [\boldsymbol{S}]^n\boldsymbol{\psi}(t). \tag{3.4}$$

The function $\boldsymbol{\psi}$ can be written in the normal form by introducing $\gamma = \ln(\sigma)/T$,

$$\boldsymbol{\psi}(t) = \exp(\gamma t)\boldsymbol{\chi}(t). \tag{3.5}$$

$\boldsymbol{\chi}(t)$ is a periodic function and γ is the characteristic exponent. The condition for instability then has the usual form $\gamma > 0$.

3.2. *Transient growth*

Transient growth has been observed in conjunction with a number of hydrodynamic instabilities, including plane channel flow, boundary layers, and isolated line vortices (Reddy & Henningson 1993; Schmid *et al.* 1992). Transient growth can also amplify small disturbances leading to nonlinear interactions in systems which are stable ($\gamma < 0$) (Trefethan *et al.* 1993). The transient growth stems from the non-normality of the linear operator governing the disturbance evolution; the operator eigenvectors are non-orthogonal. An initial condition of small magnitude can produce large expansion coefficients when projected onto the non-orthogonal eigenvectors since the eigenvectors can partially cancel each other. As the eigenmodes grow and/or decay at varying rates, the eigenvector cancellation is reduced resulting in transient growth.

The potential for transient growth can be estimated by considering the upper bound on the energy amplification (see, for example, Darmofal & Schmid 1995). For a given initial condition $\boldsymbol{\phi}(0)$, the response after n periods can be obtained by rewriting (3.2) and (3.4) in the form

$$\boldsymbol{\phi}(nT) = [\boldsymbol{A}]^n\boldsymbol{\phi}(0) = [\boldsymbol{P}][\boldsymbol{S}]^n[\boldsymbol{P}]^{-1}\boldsymbol{\phi}(0). \tag{3.6}$$

The maximum amplification after n periods $G(nT)$ for an initial input of unit norm $||\boldsymbol{\phi}(0)|| = 1$ is

$$G(nT) = \sup_{||\boldsymbol{\phi}(0)=1||} ||\boldsymbol{\phi}(nT)|| = ||[\boldsymbol{A}]^n|| = ||[\boldsymbol{P}][\boldsymbol{S}]^n[\boldsymbol{P}]^{-1}||. \tag{3.7}$$

Here we use the vector and matrix L_2-norms. The maximum amplification over all

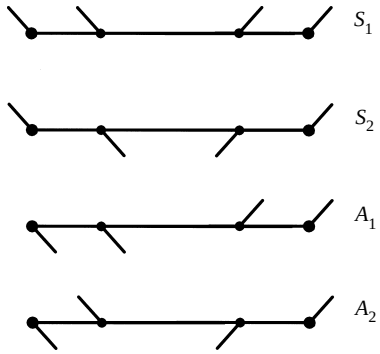

FIGURE 2. Schematic of the instability mode shapes as observed at a fixed x-position.

periods is given by

$$G_{max} \equiv \sup_{n \geqslant 0} G(nT), \tag{3.8}$$

which is bounded by

$$1 \leqslant G_{max} \leqslant \kappa |\sigma|^n_{max}; \tag{3.9}$$

κ is the condition number of the matrix $[\boldsymbol{P}]$ and $|\sigma|_{max}$ is the magnitude of the maximum eigenvalue of $[\boldsymbol{A}]$.

The condition number κ provides an indicator of the potential for transient growth. When $\kappa = 1$, the eigenvectors are orthogonal and there is no transient growth. The maximum amplification is then completely governed by instability. For $\kappa > 1$, transient growth can occur. To estimate the level of transient growth, we consider the maximum amplification $G(T)$ over the first period of vortex motion. This requires an evaluation of the matrix norm $||[\boldsymbol{A}]||$.

4. Stability and transient-growth characteristics

The mean-position and perturbation equations are integrated numerically in order to define the matrix $[\boldsymbol{A}]$. The first few points are evaluated using a forth-order Runge–Kutta scheme; the remaining steps are evaluated using the Adams–Bashforth predictor scheme. The stability results are based on a time step of $\Delta t = 0.01$. Further reduction in Δt changes the growth rate by less than 1%.

4.1. *Instability mode shapes*

The eigenvectors corresponding to different values of σ describe the relative magnitudes and orientations of the perturbations on each of the vortices. Following Crow (1970), we classify the modes as symmetric or antisymmetric based on their appearance from the ground. A mode which is symmetric with respect to the vortices 1 and 2 satisfies the condition $\eta_1 = -\eta_2$ and $\zeta_1 = \zeta_2$. The corresponding antisymmetric mode satisfies the condition $\eta_1 = \eta_2$ and $\zeta_1 = -\zeta_2$. Considering the complete system of four vortices, we define two symmetric modes S_1, S_2, and two antisymmetric modes A_1, A_2, as shown in figure 2. The diagrams show the relative orientation of the disturbances at a single x-location at a time nT, $n \geqslant 1$. This is quantified by the angles $\theta_2 = \tan^{-1}(\zeta_2/\eta_2)$ and $\theta_4 = \tan^{-1}(\zeta_4/\eta_4)$. The relative magnitudes are given by the ratio $|\eta_4/\eta_2|$.

The modes S_1 and A_1 are generalizations of the Crow instability modes. The vorticity centroids are perturbed in a direction consistent with a single vortex at the

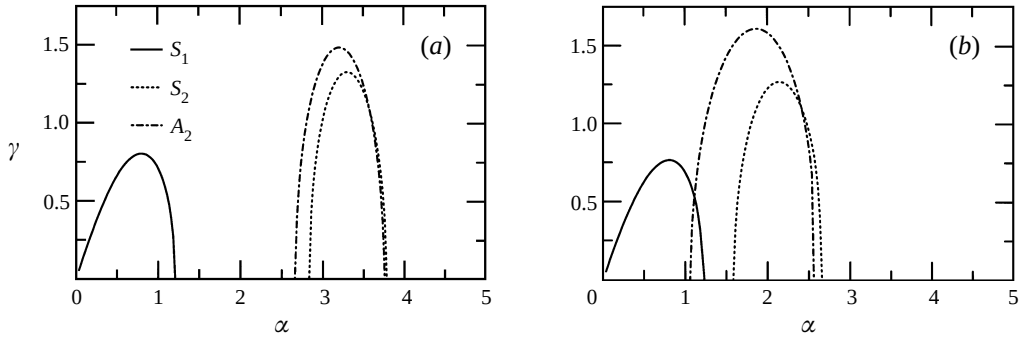

FIGURE 3. Growth rate γ as a function of wavenumber α for different values of the vortex-spacing parameter (*a*) $\delta = 0.3$, (*b*) $\delta = 0.4$ with $\Gamma = 0.5$, $\epsilon = 0.05$.

centroid location. The modes S_2 and A_2 are perturbations about the centroids. The centroid locations are only weakly perturbed.

4.2. *Growth rates*

Figure 3 shows the variation of the growth rate γ with the wavenumber α for two values of the spacing parameter δ. The range $0.3 \leqslant \delta \leqslant 0.4$ covers typical values for commercial aircraft; for smaller values of δ, the co-rotating vortices are more likely to merge. The circulation ratio $\Gamma = 0.5$ and cutoff parameter $\epsilon = 0.05$ are constant. The results show three unstable modes: S_1, S_2, and A_2. The variation of the growth rate for the S_1 mode is similar to the long-wavelength Crow instability for a single vortex pair placed at the vorticity centroids. This mode is only weakly affected by changes in the co-rotating-vortex spacing δ. The maximum growth rate is approximately 0.8. For $\delta = 0.3$ and $\alpha = 0.8$, the orientation of the S_1 mode after $t = nT$ is given by $\theta_2 = 45°$, $\theta_4 = 52°$, $|\eta_4/\eta_2| = 0.9$. The orientation does not change significantly during the rotation period T, as discussed in §5.1.

The modes S_2 and A_2 are shorter-wavelength instabilities. These modes are quite sensitive to the vortex-spacing parameter δ. The most unstable wavenumbers decrease from $\alpha \approx 3.3$ at $\delta = 0.3$ to $\alpha \approx 2$ at $\delta = 0.4$. The antisymmetric mode A_2 has a maximum growth rate of approximately 1.5 and the symmetric mode S_2 has a maximum growth rate close to 1.3. For $\delta = 0.3$ and $\alpha = 3.3$, the orientation of the S_2 mode at $t = nT$ is given by $\theta_2 = 67°$, $\theta_4 = -110°$, $|\eta_4/\eta_2| = 2.6$. The orientation of the A_2 mode with $\alpha = 3.2$ is given by $\theta_2 = 68°$, $\theta_4 = -111°$, $|\eta_4/\eta_2| = 3.0$. The orientation of these modes changes significantly over the rotation period T. When the vortices are aligned along $z = 0$ (i.e. $t = nT/2$), the ζ perturbation is larger than the η perturbation. When the vortices are aligned along $y = 0.5$ (i.e. $t = T/4 + nT/2$), the η perturbation is largest. This is demonstrated by the numerical-integration results of §5.2. The peak growth rates for both the A_2 and S_2 modes are substantially larger than for the S_1 mode.

The S_2 and A_2 modes should not be confused with the spurious short-wavelength modes found by Crow (1970) for $\alpha\epsilon \approx 1$ (using our notation). Widnall, Bliss & Tsai (1974) show that the thin-filament analysis is limited to wavelengths which are large compared to the core size $\alpha\epsilon \ll 1$, and that spurious instabilities are predicted for $\alpha\epsilon \approx 1$. In the current analysis, the shorter-wavelength modes are observed for $\alpha\epsilon < 0.05$, which is within the range of validity of the long-wavelength approximation.

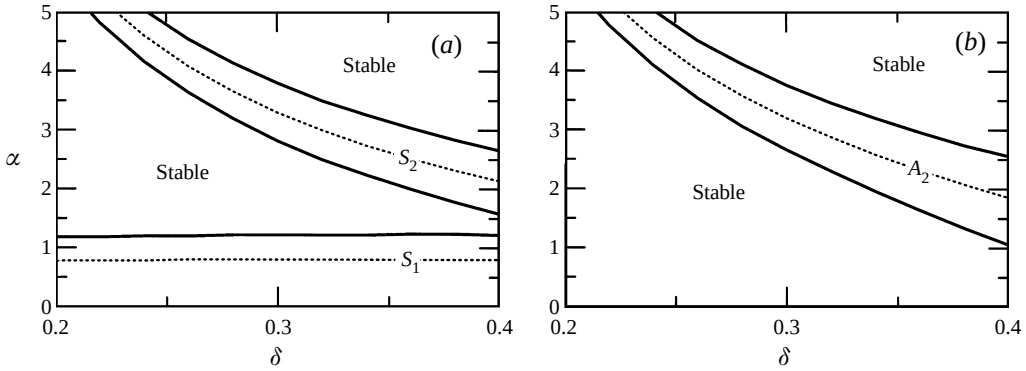

FIGURE 4. Neutral-stability diagrams for (*a*) symmetric and (*b*) antisymmetric modes with $\Gamma = 0.5$, $\epsilon = 0.05$.

In addition, the wavenumber α for the S_2 and A_2 modes increases with increasing ϵ – in contrast to the spurious modes.

Focusing on the S_1 mode, figure 3 shows that the maximum growth rate is slightly reduced and the most unstable wavenumber is slightly increased due to increased δ. These quantities are non-dimensionalized by the total circulation $\widetilde{\Gamma}_0$ and the spacing between vorticity centroids $\tilde{b}$. To estimate the effects of Γ and δ on the physical growth rate we consider lift distributions with the tip vortices separated by a fixed distance $\tilde{b}^*$ (i.e. constant span). As the strength and position of the flap vortex is changed, the total lift is held constant. For $\Gamma = 0$, there is a single vortex pair of strength $\widetilde{\Gamma}_0^*$ separated by $\tilde{b}^*$. For $\Gamma \neq 0$, constant lift requires $\widetilde{\Gamma}_0\tilde{b} = \widetilde{\Gamma}_0^*\tilde{b}^*$. This provides a relationship between $\tilde{b}^*$ and $\tilde{b}$ and $\widetilde{\Gamma}_0^*$ and $\widetilde{\Gamma}_0$. The physical growth rate γ^* (non-dimensionalized by fixed values $\widetilde{\Gamma}_0^*$ and $\tilde{b}^*$) is related to the growth rate parameter γ through the relation $\gamma^*/\gamma = [1 + 2\delta(\Gamma/(1+\Gamma))]^3$. For $\delta = 0.3$, an increase in Γ from 0.25 to 0.75 results in a 40% increase in the physical growth rate. Although the growth rate parameter γ is relatively unchanged with Γ and δ, the physical growth rate for a constant-lift/constant-span configuration can change by more than a factor of 2.

4.3. *Neutral-stability curves*

The peak growth rates for the various modes show little change with the parameters Γ, δ, and ϵ. However, the band of unstable wavenumbers, α, changes significantly with these parameters as shown by figure 3. Here we consider the neutral-stability curves that define the instability boundaries for the dominant modes. Figure 4 shows the neutral-stability curves in the (δ, α)-plane for symmetric and antisymmetric modes with fixed values of $\Gamma = 0.5$ and $\epsilon = 0.05$. The dashed lines show the location of maximum growth. The S_1 mode shows little variation with δ. The S_2 mode shows a shift toward smaller wavenumbers for larger δ. The instability band for the A_2 mode corresponds roughly with the S_2 mode, just as for figure 3. There is an increase in the bandwidth for the S_2 and A_2 instabilities as the spacing parameter δ is increased. For $\delta = 0.4$, both the S_1 and A_2 modes are unstable for $\alpha \approx 1.1$.

Figure 5 shows neutral curves for a smaller core size, $\epsilon = 0.02$. The primary effect of the smaller core size on the S_1 mode is to shift the instability to smaller wavenumbers. The wavenumbers of the unstable S_2 and A_2 modes show an even larger decrease with decreasing core size. The maximum growth rates (not shown)

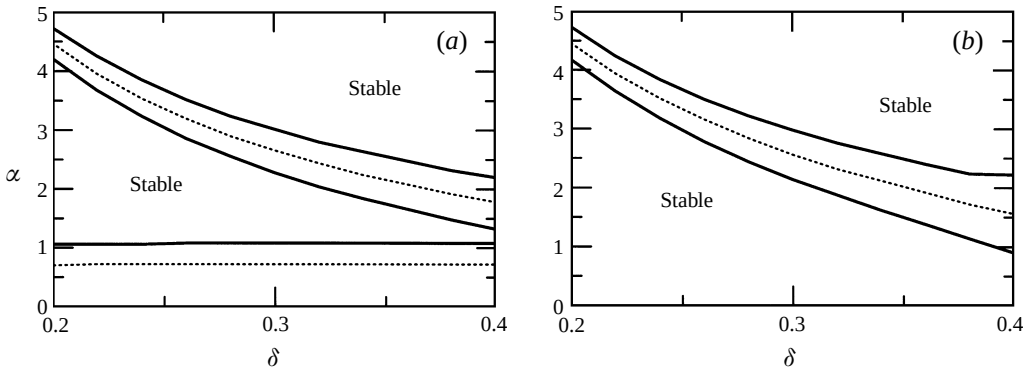

FIGURE 5. Neutral-stability diagrams for (*a*) symmetric and (*b*) antisymmetric modes with $\Gamma = 0.5$, $\epsilon = 0.02$.

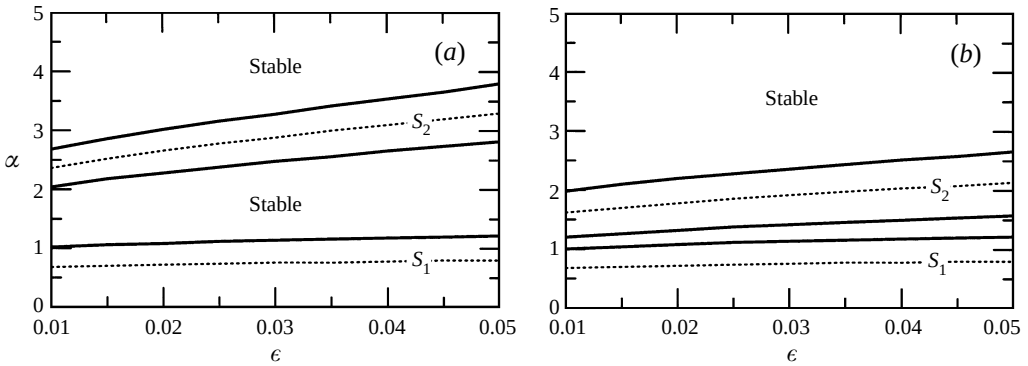

FIGURE 6. Neutral-stability diagrams for symmetric modes with $\Gamma = 0.5$ and (*a*) $\delta = 0.3$, (*b*) $\delta = 0.4$.

display no significant variation with ϵ. The bandwidth for the A_2 and S_2 modes increases with increasing core size. Figure 6 shows the instability boundaries in the (ϵ, α)-plane for the symmetric modes with $\delta = 0.3$ and $\delta = 0.4$. The effect of the core size on the S_1 mode is similar to the results for a single vortex pair (Crow 1970). The S_2 mode (and the A_2 mode, not shown) shows a greater sensitivity to the core size. However, this sensitivity is reduced when the spacing parameter is increased. A factor of 2 increase in the core size would not significantly shift the band of most-unstable wavenumbers.

Variation of the circulation ratio Γ has a similar effect to changing ϵ. For $\epsilon = 0.2$, increasing Γ from 0.5 to 1 shifts the wavenumber for maximum growth of the S_2 and A_2 modes by $\Delta\alpha \approx -0.1$. Decreasing Γ from 0.5 to 0.25 shifts the wavenumber for maximum growth by $\Delta\alpha \approx 0.5$. Part of the effect of changing Γ is due to the change in the cutoff length for vortices 1 and 3 as discussed in §2.1.

4.4. *Maximum amplification for transient growth*

The condition number κ, in conjunction with the most unstable eigenmode, provides an upper bound for the disturbance amplification from any initial conditions at a given wavenumber α. For $\kappa = 1$, the disturbance amplification is completely governed

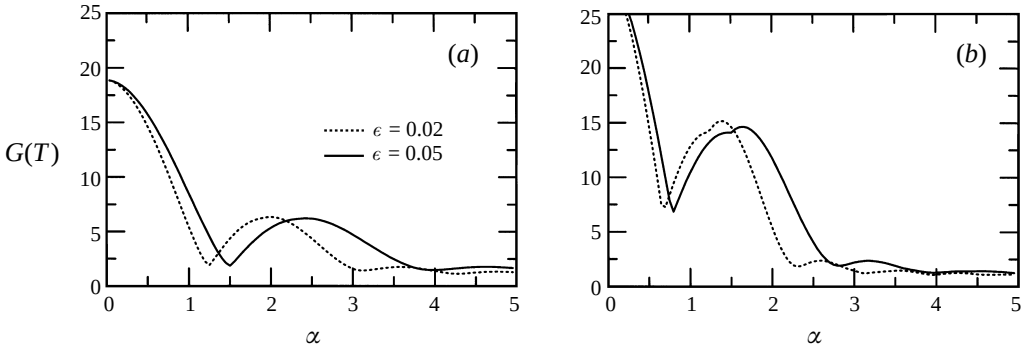

FIGURE 7. Maximum amplification $G(T)$ as a function of wavenumber α for different values of the cutoff parameter ϵ with vortex-spacing parameter values (*a*) $\delta = 0.3$, $T = 0.634$, (*b*) $\delta = 0.4$, $T = 1.28$, and $\Gamma = 0.5$.

by instability and there is no transient growth; for $\kappa > 1$, transient growth can occur. The system of two trailing-vortex pairs is characterized by $\kappa > 1$ – indicating the potential for transient growth – for most wavenumbers of interest. The maximum amplification after one period $G(T)$ provides a measure for the level of potential transient amplification.

Figure 7 shows the maximum amplification $G(T) = ||[\boldsymbol{A}]||$ as a function of α for different values of ϵ and δ. The values of $G(T)$ at different δ are not directly comparable since they represent different instances in time: for $\delta = 0.3$, $T = 0.634$ and for $\delta = 0.4$, $T = 1.28$. If there is no transient amplification, $\kappa = 1$, then $G(T)$ is the result of instability. Using the results of figure 3, the maximum instability amplification over one period is approximately 3 for $\delta = 0.3$, and 8 for $\delta = 0.4$. At wavenumbers below $\alpha \approx 1$, the maximum instability growth over one period is only about 2 for $\delta = 0.3$, and about 3 for $\delta = 0.4$. Thus figure 7 shows a strong potential for transient growth.

The largest level of transient amplification occurs at small α. At large values of α, there is negligible transient growth ($G(T) \approx 1$). The level of transient amplification is insensitive to the vortex core size ϵ, except for a slight shift in wavenumbers. The minima in $G(T)$ at $\alpha \approx 1.4$ for $\delta = 0.3$, and $\alpha \approx 0.7$ for $\delta = 0.4$, correspond to conditions where the maximum amplification occurs at $t \approx T/2$.

For $\delta = 0.3$, $G(T) \approx 12$ at wavenumbers close to maximum growth of the S_1 mode. This suggests that the disturbance growth rate over short time intervals can be five times greater than the level predicted by linear stability theory. A similar result is obtained for $\delta = 0.4$ for wavenumbers slightly less than the most unstable.

5. Numerical-integration results

The temporal evolution of the vortex positions and the disturbance amplitudes can be studied by numerically integrating the initial-value problem (2.32)–(2.37). A combination of Runge–Kutta and Adams–Bashforth schemes are used with a time step $\Delta t = 0.01$. The results shown in this section are for a circulation ratio of $\Gamma = 0.5$ and a co-rotating-vortex spacing of $\delta = 0.3$. The initial positions are consistent with figure 1. Vortices 2 and 4 follow a nearly circular orbit about ($y = 0.5$, $z = 0$) in the local reference frame. The period of orbit is $T = 0.634$; this is larger than

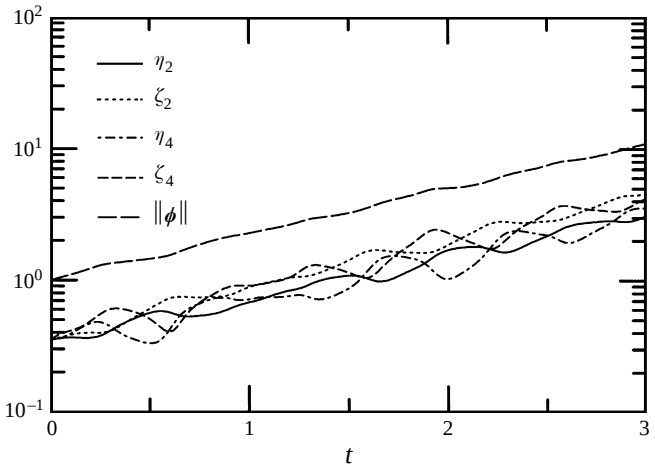

FIGURE 8. Amplitude growth curves for an S_1 mode with $\Gamma = 0.5$, $\epsilon = 0.05$, $\delta = 0.3$, $\alpha = 0.7$ and initial conditions $\boldsymbol{\phi}(0) = (-1, 1, -1, 1, 1, 1, 1, 1)/\sqrt{8}$.

$2\pi\delta^2 = 0.565$ due to the interaction with vortices 1 and 3. The smaller vortex follows a larger trajectory around the vorticity centroid.

5.1. S_1 *modes*

We first consider the evolution of an S_1 symmetric mode at a wavenumber of $\alpha = 0.7$. Figure 8 shows the variation of the perturbations η_2, ζ_2, η_4, ζ_4 and the norm $||\boldsymbol{\phi}||$. The initial condition $\boldsymbol{\phi}(0) = (-1, 1, -1, 1, 1, 1, 1, 1)/\sqrt{8}$ is symmetric with $\theta_2 = \theta_4 = 45°$, $\eta_4/\eta_2 = 1$ and $||\boldsymbol{\phi}(0)|| = 1$. After some initial adjustment, the disturbance growth is characteristic of the predicted unstable eigenmode for these conditions. At $t = 2$ (after the vortex centroids have propagated a distance $2\tilde{b}$), the disturbance has grown by a factor of 5.

Superposed on the instability growth (shown by the norm) is a periodic variation of the various perturbation components. The dominant period for this variation is $T = 0.634$, the period of orbit for the co-rotating pair. As vortices 2 and 4 (and 1 and 3) propagate about one another, the orientation of the instability changes slightly. However, the primary orientation of the perturbation remains essentially the same since the magnitudes of the variations are only about 10% of the amplitudes.

The orientation of the perturbations is most clearly seen in figure 9, which shows the vortices (1, 2, 3 and 4) at four different times in the co-rotating-vortex period: $t = T/4$, $t = T/2$, $t = 3T/4$, $t = T$. The initial amplitude is $||\boldsymbol{\phi}(0)|| = 0.1$. The length of the vortex sample shown is $x = 10$, about 1.1 wavelengths. The lower-right ends of the vortices are at the perturbation nodes, so they show the unperturbed vortex positions. The perturbations remain aligned along $\theta_2 = \theta_4 \approx 45°$ with $\eta_4/\eta_2 \approx 1$. Thus the vorticity centroids on the starboard and port sides are roughly aligned consistent with the Crow instability.

5.2. S_2 *and* A_2 *modes*

Both the S_2 and A_2 modes are dominated by perturbations about the vorticity centroids. Here we focus on the symmetric S_2 mode. Figure 10 shows the variation of the perturbation magnitudes η_2, ζ_2, $-\eta_4$, $-\zeta_4$ and the norm $||\boldsymbol{\phi}||$ at the wavenumber $\alpha = 3.3$. The negative values are shown since η_4, $\zeta_4 < 0$, as seen in figure 2. The initial

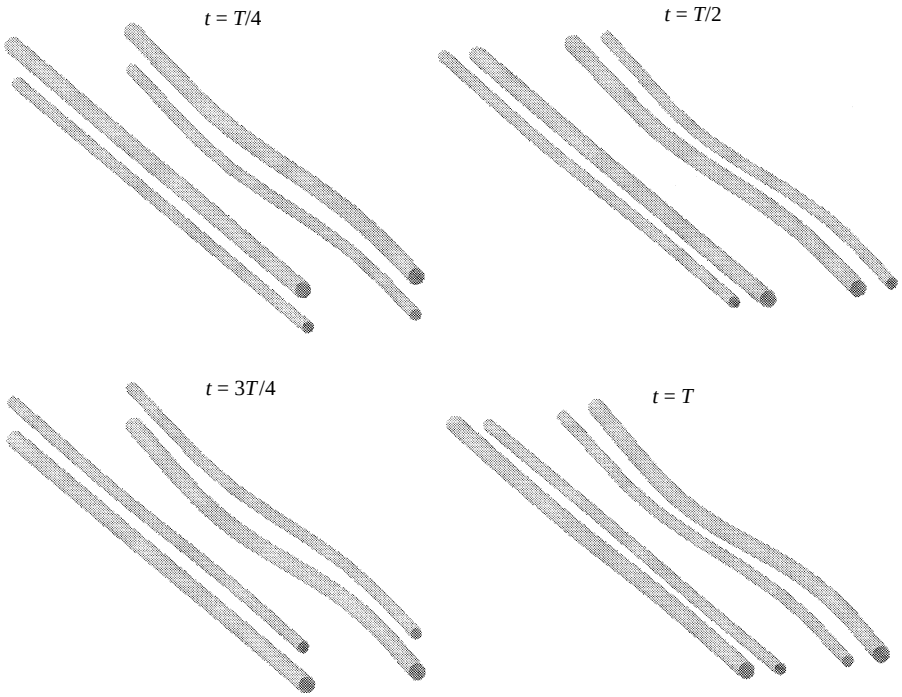

FIGURE 9. Oblique view of vortices with growing S_1 mode at $t = T/4$, $t = T/2$, $t = 3T/4$, $t = T$ for the conditions of figure with $||\boldsymbol{\phi}(0)|| = 0.1$.

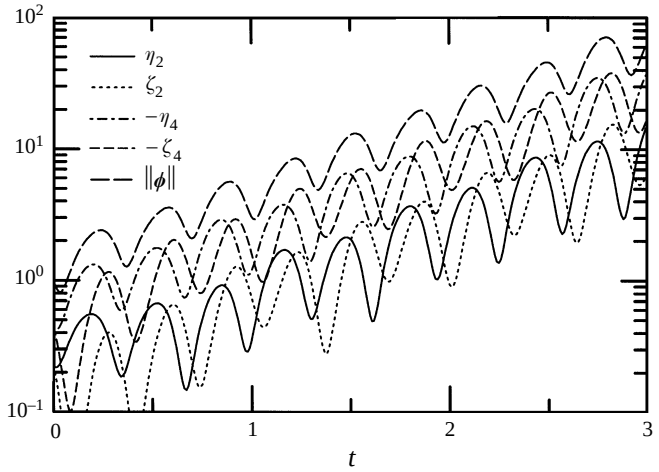

FIGURE 10. Amplitude growth curves for an S_2 mode with $\Gamma = 0.5$, $\epsilon = 0.05$, $\delta = 0.3$, $\alpha = 3.3$ and initial conditions $\boldsymbol{\phi}(0) = (-1, 1, 2, -2, 1, 1, -2, -2)/\sqrt{20}$.

condition $\boldsymbol{\phi}(0) = (-1, 1, 2, -2, 1, 1, -2, -2)/\sqrt{20}$ is symmetric with $\theta_2 = 45°$, $\theta_4 = -135°$, $\eta_4/\eta_2 = 2$ and $||\boldsymbol{\phi}(0)|| = 1$. The perturbation quickly adjusts to the predicted growth rate and eigenmode shape. The relative magnitudes of the perturbations are inversely proportional to the circulation strengths of the vortices. By $t = 2$, the

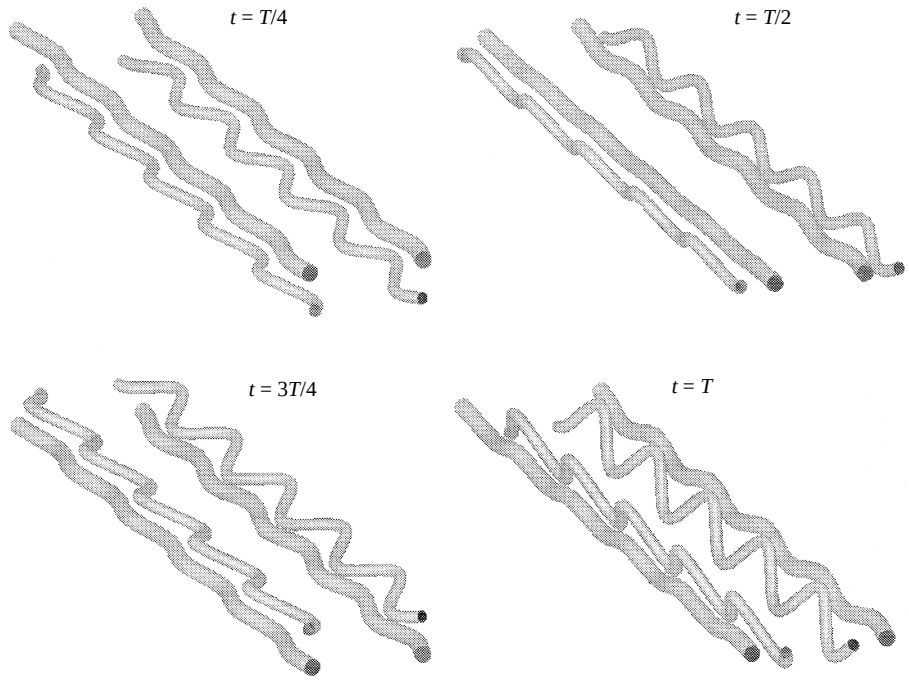

FIGURE 11. Oblique view of vortices with growing S_2 mode at $t = T/4$, $t = T/2$, $t = 3T/4$, $t = T$ for the conditions of figure with $||\boldsymbol{\phi}(0)|| = 0.1$.

disturbance has grown by a factor 10 to 20 (depending on the instantaneous vortex positions).

Unlike the S_1 mode, the norm of the S_2 mode undergoes a factor of 2 variation over the orbit period of the co-rotating pair. The various perturbation components undergo even larger variations over the rotation period. These large variations correspond to changes in the perturbation orientation. This can be seen in figure 11 which shows the vortices with $||\boldsymbol{\phi}(0)|| = 0.1$ at four different times in the co-rotating-vortex period: $t = T/4$, $t = T/2$, $t = 3T/4$, $t = T$. The length of the vortex sample shown is $x = 10$ (the same as for figure 9), about 5.2 wavelengths for the S_2 mode. Again, the lower-right ends of the vortices show the unperturbed vortex positions. Viewed from the end, the vortex perturbations maintain the same basic orientation over the complete period (i.e. upward and outward, and inward and downward, as shown in figure 2). However, when the vortices are aligned at $y = \pm 0.5$, the perturbations are largest in the y-direction. When the vortices are aligned along $z = 0$, the perturbations are largest in the z-direction. The disturbance growth results from a balance of self-induction, mutual induction from the co-rotating vortex, and mutual induction from the counter-rotating vortices.

5.3. *Transient growth*

The analysis and results of §§3.2 and 4.4, respectively, show the potential for significant transient growth in the two-vortex-pair system. The level of amplification that occurs depends on the initial conditions. Figure 12 shows the disturbance-amplitude evolutions for the conditions of figure 8 with initial conditions $\boldsymbol{\phi}(0) = (-1, 1, 0, 0, 1, 1, 0, 0)/\sqrt{4}$ (i.e. $\eta_4/\eta_2 = 0$ instead of $\eta_4/\eta_2 = 1$). These initial conditions

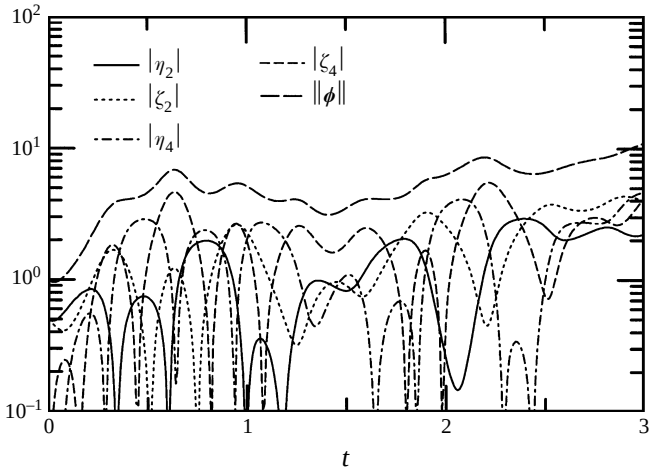

FIGURE 12. Amplitude growth curves showing transient growth with $\Gamma = 0.5$, $\epsilon = 0.05$, $\delta = 0.3$, and $\alpha = 0.7$ and initial conditions $\boldsymbol{\phi}(0) = (-1, 1, 0, 0, 1, 1, 0, 0)/\sqrt{4}$.

lead to transient growth which amplifies the disturbance by a factor of 5 from $t = 0$ to $t = 0.55$. Thus the transient growth produces the same level of amplification as the instability in approximately a quarter of the time. At large times, the disturbance amplitudes vary in accordance with the unstable eigenmode. By exciting only the outboard vortices (1 and 2), the short-term growth is dramatically increased.

The form of the perturbation during transient growth is quite different from the unstable eigenmode at this wavenumber. These differences can be seen in the strong periodic variations in the perturbation amplitudes of figure 12. Figure 13 shows the vortices at the times $t = T/4$, $t = T/2$, $t = 3T/4$, $t = T$, for the conditions of figure 12 with $||\boldsymbol{\phi}(0)|| = 0.1$. The length of the vortex sample is again $x = 10$ (about 1.1 wavelengths). Most of the perturbation is about the vorticity centroids, in contrast with the S_1 mode. The alignment of the perturbations during the co-rotating-vortex period resembles the S_2 mode. The vortices within a given pair, 2 and 4 or 1 and 3, are perturbed in planes that are roughly parallel. The orientation of these planes rotates as the vortices propagate about one another.

6. Summary and conclusions

The stability analysis for a system of two trailing-vortex pairs shows three different growth mechanisms that may influence the final break up of the vortices. The first mechanism is a long-wavelength instability. This is a generalization of the symmetric Crow (1970) instability that accounts for the co-rotation produced by two vortex pairs. The mode shapes are characterized by displacements of the vorticity centroids. Unstable wavelengths are greater than five times the vorticity centroid spacing $\tilde{b}$. Maximum growth rates, non-dimensionalized by the total circulation and the centroid spacing, are approximately 0.8. The growth rates are in close agreement with those predicted for a single vortex pair. The spacing and relative circulation between the flap and tip vortices provides only a small modification of the non-dimensional growth rate. However, the physical growth rate (for a constant-lift/constant-span configuration) can vary by more than 50% for different values of the spacing and

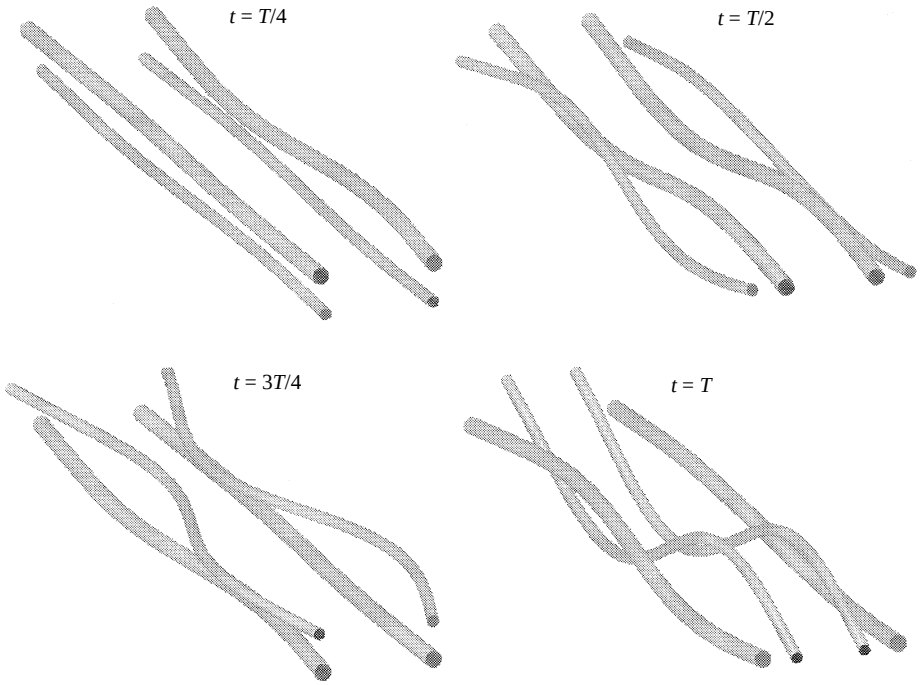

FIGURE 13. Oblique view of vortices showing transient growth at $t = T/4$, $t = T/2$, $t = 3T/4$, $t = T$ for the conditions of figure 12 with $||\phi(0)|| = 0.1$.

relative circulation. This results from the changes in the vorticity centroid spacing and the total circulation.

The second growth mechanism identified for the two-vortex-pair system is short-wavelength instabilities. The results show both symmetric and antisymmetric modes. These modes are characterized by displacements about the vorticity centroids, with the centroid locations relatively unperturbed. The band of unstable wavelengths for these modes depends on the vortex-core size and the flap- and tip-vortex spacing and circulation ratio. For the parameters considered, the symmetric-mode wavelength lies between $1.5\tilde{b}$ and $4\tilde{b}$. The antisymmetric mode wavelength lies between $1.5\tilde{b}$ and $6\tilde{b}$. Although these wavelengths are shorter than the symmetric Crow instability mode, they are long relative to the effective vortex-core size. Maximum growth rates are approximately 1.3 for the symmetric mode and 1.6 for the antisymmetric mode.

The third growth mechanism identified for the two vortex pairs is transient growth. Wavelengths associated with the long-wavelength instability show the greatest potential for transient growth. The amount of amplification depends on the initial conditions. Exciting both vortex pairs, so that the distribution of the initial perturbation is close to the most unstable mode, results in very little transient growth. If, however, only one vortex pair is excited, significant transient growth is observed. The transient growth can amplify an initial disturbance by a factor of 10 to 15 over one period of rotation of the co-rotating pair (one fifth of the time required for comparable growth due to instability at the same wavelength).

For comparison purposes, we consider the distance required for a factor of 10 amplification behind a 747-400 aircraft. The non-dimensional approach speed for the 747 is $V_A \approx 40$; the airplane travels 40 spans in the time that the vortex centroids

descend 1 span. The vortex-centroid spacing is taken to be $\pi/4$ spans. One non-dimensional time unit ($t = 1$) then corresponds to 31 spans behind the aircraft. The flap and tip vortices would undergo one period of rotation in approximately 40 spans. For the S_1 long-wavelength mode, a perturbation is amplified by a factor of 10 at 90 spans behind the aircraft. The S_2 and A_2 short-wavelength modes undergo the same amplification by 56 spans and 45 spans, respectively. Transient growth associated with the long-wavelength S_1 mode can amplify by a factor of 10 within a distance of 30 spans behind the aircraft.

These mechanisms are relevant to the vortex behaviour behind lifting bodies in flaps-down high-lift configurations. These configurations produce multiple trailing-vortex pairs. The relative significance of the different mechanisms will depend on the length of time that distinct co-rotating vortices persist, on the initial conditions feeding into the instabilities, and on the effects of nonlinear distortion to the amplified perturbations.

Philippe Spalart and Byram Bays-Muchmore of Boeing and Peter Schmid of the University of Washington provided a number of helpful discussions. A version of this paper was presented as *AIAA Paper* 97-0062.

REFERENCES

Bruin, A. C. de, Hegen, S. H., Rohne, P. B. & Spalart, P. R. 1996 Flow field survey in trailing vortex system behind a civil aircraft model at high lift. In *The Characterization and Modification of Wakes From Lifting Vehicles in Fluids*, pp. 25/1–12. AGARD CP-584.

Caiger, B. & Gould, D. G. 1971 An analysis of flight measurements in the wake of a jet transport aircraft. In *Aircraft Wake Turbulence and its Detection* (ed. J. Olsen, A. Goldburg & M. Rogers), pp. 125–136. Plenum.

Crouch, J. D. 1996 Stability of multiple trailing-vortex pairs. In *The Characterization and Modification of Wakes From Lifting Vehicles in Fluids*, pp. 17/1–8. AGARD CP-584.

Crow, S. C. 1970 Stability theory for a pair of trailing vortices. *AIAA J.* **8**, 2172–2179.

Crow, S. C. & Bate, E. R. 1976 Lifespan of trailing vortices in a turbulent atmosphere. *J. Aircraft* **13**, 476–482.

Darmofal, D. L. & Schmid, P. J. 1995 The importance of eigenvectors for local preconditioners of the Euler equations. *AIAA Paper* 95-1655-CP.

Dunham, R. E. 1974 Model tests of various vortex dissipation techniques in a water towing tank. *NASA LWP*-1146.

Fell, St. & Staufenbiel, R. 1995 Formation and structure of vortex systems generated by unflapped and flapped wing configurations. *Z. Flugwiss. Weltraumforsch.* **19**, 366–379.

Hackett, J. E. & Evans, P. F. 1977 Numerical studies of three-dimensional breakdown in trailing vortex wakes. *J. Aircraft* **14**, 1093–1101.

Jacob, J. D. & Savas, Ö. 1997 Vortex dynamics in trailing wakes of flapped rectangular wings. *AIAA Paper* 97-0048.

Jimenez, J. 1975 Stability of a pair of co-rotating vortices. *Phys. Fluids* **18**, 1580.

Klein, R., Majda, A. J. & Damodaran, K. 1995 Simplified equations for the interaction of nearly parallel vortex filaments. *J. Fluid Mech.* **288**, 201–248.
vortex-wake decay",

Moore, D. W. & Saffman, P. G. 1972 The motion of a vortex filament with axial flow. *Phil. Trans. R. Soc. Lond.* A **272**, 403–429.

Nayfeh, A. H. & Mook, D. T. 1979 *Nonlinear Oscillations*. Wiley & Sons.

Reddy, S. C. & Henningson, D. S. 1993 Energy growth in viscous channel flows. *J. Fluid Mech.* **252**, 209–238.

Rossow, V. J. 1977 Convective merging of vortex cores in lift-generated wakes. *J. Aircraft* **14**, 283–290.

Sarpkaya, T. & Daly, J. J. 1987 Effect of ambient turbulence on trailing vortices. *J. Aircraft* **24**, 399–404.

Schmid, P. J., Henningson, D. S., Khorrami, M. R. & Malik, M. R. 1992 Sensitivity analysis of hydrodynamic stability operators. *ICASE Rep.* 92-33.

Snedeker, R. S. & Bilanin, A. J. 1975 Analysis of the vortex wakes of the Boeing 727, Lockheed L-1011, McDonnell Douglas DC-10, and Boeing 747 Aircraft. *Rep. 245*. Aeronautical Research Associates of Princeton, Inc.

Spalart, P. R. & Wray, A. A. 1996 Initiation of the Crow instability by atmospheric turbulence. In *The Characterization and Modification of Wakes From Lifting Vehicles in Fluids*, pp. 18/1–8. AGARD CP-584.

Trefethan, L. N., Trefethan, A. E., Reddy, S. C. & Driscoll, T. A. 1993 Hydrodynamic stability without eigenvalues. *Science* **261**, 578.

Widnall, S. E. 1975 The structure and dynamics of vortex filaments. *Ann. Rev. Fluid Mech.* **7**, 141–165.

Widnall, S. E., Bliss, D. B. & Tsai, C. Y. 1974 The instability of short waves on a vortex ring. *J. Fluid Mech.* **66**, 35–47.

Widnall, S. E., Bliss, D. & Zalay, A. 1971 Theoretical and experimental study of the stability of a vortex pair. In *Aircraft Wake Turbulence and its Detection* (ed. J. Olsen, A. Goldburg & M. Rogers), pp. 305–338. Plenum.